

Symmetry and scale orient Min protein patterns in shaped bacterial sculptures

Fabai Wu, Bas van Schie, Juan E. Keymer, Cees Dekker*

* To whom correspondence should be addressed. Email: c.dekker@tudelft.nl

This file includes:

Supplementary Methods
Supplementary Discussions
Supplementary Figures 1 to 16
Supplementary Tables 1 to 4
Descriptions for Supplementary Movie 1 to 12
References

Supplementary Methods

Plasmid and strain construction

All primers are listed in Supplementary Table 2. All plasmid and strain descriptions are provided in Supplementary Table 3.

(i) Labeling endogenous *minD* gene (Supplementary Fig. 3a):

Plasmid pBVS3 was constructed by using an Infusion kit (Clontech) to combine two PCR products respectively amplified from pFX40 (primers 1413 and 1215) and an intermediate plasmid containing MinDE::kanR *frt* cassette (primers 1410 and 1312).

Plasmid pBVS4 was constructed by replacing the *yfp* gene with a bacteria-codon optimized *sfgfp* gene¹ through an Infusion kit, combining the PCR products of pBVS3 (primers 1473 and 1474) and psfGFP (primers 1471 and 1472).

Bacterial strain W3110 was made competent by a Mix&Go transformation kit (Zymoresearch) and transformed with plasmid pKD46. This strain was then transformed with linear fragments containing a *cat::sacB* cassette PCR-amplified from pKD3V (primers 1206 and 1207) to replace *minD minE* genes via λ Red recombination, and selected for transformants resistant to chloramphenicol and sensitive to sucrose. This resulted in strain FW1363. The *cat::sacB* was replaced via λ Red recombination² by a PCR product containing the *sfgfp::minD minE::frt kanR frt* cassette from pBVS4 (primers 1485 and 1135), leading to strain FW1541. This strain is then transformed with pCP20, and the kanR gene was removed by the flippase during growth at 42°C, resulting in strain FW1555.

(ii) Labeling the cytosol with constitutively expressed eqFP670³ (commercial name NirFP):

A first strain with genomic insertion of TagBFP was constructed. The constructs were constructed via *in vitro* site-specific recombination. PCR products containing *lacI::Pt7, tagBFP, eqFP670* and *frt-kanR-frt* respectively from pET-15a (primers 929 and 944), pTagBFP-C1 (930 and 945), pNirFP-N1 (primers 937 and 952) and pKD13 (primers 940 and 955) were inserted in the entry plasmids via Gateway BP reactions to result in pBVS7, pBVS19, pBVS15 and pBVS17, respectively. Plasmids pBVS7, pBVS19 and pBVS17 were then recombined into Gateway destination vector via Gateway LR reaction kits (Invitrogen), to result in pBVS35. PCR products of pBVS35 (primers 1013 and 1020) with 5' extension of a synthetic sequence of promoter Pj23100 from Anderson collection (<http://parts.igem.org/Promoters/Catalog/Anderson>) was recombined into the *leuB* locus of W3110 strain to result in strain FW1247.

To construct the *Pj23100::eqFP670::kanR* plasmid, we also used *in vitro* site-specific recombination. PCR products from FW1247 with the promoter sequence *Pj23100* with a 200 basepair (bp) genomic sequence upstream (primers 1326 and 1327), and the *kanR frt* with a 200 bp sequence downstream (primers 940 and 1328) were separately amplified to produce pBVS28 and pBVS29. These two plasmids were then mixed with pBVS15 and the pDEST R4-R3 to produce pBVS33 using Gateway LR reaction. A PCR product of pBVS33 (primers 1238 and 1239) containing the homology sequence to the *leuB* locus (200bp at each side) and the *Pj23100::eqFP670::kanRfrt* cassette was inserted into the genome of the W3110 strain via λ Red recombination to produce strain FW1489.

The *Pj23100::eqFP670::kanRfrt* cassette was transduced into strain FW1555 via P1 transduction using a P1 phage, a kind gift from Ariel Lindner. This resulted in a strain FW1590 for all lab-on-a-chip experiments in this study. All strains above were verified by antibiotic sensitivity, PCR (Phusion polymerase, Thermo Scientific), sequencing (BaseClear) and confirmed by microscopy for fluorescence, a minicelling phenotype (Δ MinDE) or a restoration from minicelling phenotype.

The strains W3110, FW1363, FW1489, FW1555, and FW1590 were used to measure growth rate and/or western blot to compare the effect of full-length MinDE knockout, expression of eqFP670, and the expression of sfGFP-MinD. The promoters and ribosome-binding sites of *minC*, *minD* and *minE* are all unperturbed in all the resulting strains. Expression of eqFP670 and sfGFP-MinD are shown not to affect the growth rate of the cells (Supplementary Fig. 3d).

In these strains, the MinD and MinE genes are co-transcribed at their endogenous locus. The cells in our study are polyploid, with chromosome numbers that scale with cell size. Therefore, the MinD/MinE concentrations will be roughly constant across the large variation in cell volumes studied.

Culture conditions

For genetic engineering, *E. coli* cells were incubated in Lysogeny broth (LB) supplemented, when required, with 100 µg/ml ampicillin (Sigma-Aldrich), 50 µg/ml kanamycin (Sigma-Aldrich), or 34 µg/ml chloramphenicol (Sigma-Aldrich) for plasmid selection, or with 25 µg/ml kanamycin, 20 µg/ml chloramphenicol, or 0.2% sucrose for selection of the genomic insertions of gene cassettes. For growth rate measurements and for cell-sculpting, we used M9 minimum medium (Fluka Analytical) supplemented with 2 mM MgSO₄, 0.1mM CaCl₂, 0.4% glucose (Sigma-Aldrich), and 0.25% protein hydrolysate amicase (Fluka Analytical). For growth rate measurements, overnight cultures were back diluted in triplicates to optical density (OD600) = 0.02 in flasks containing 100 ml of M9 medium with supplements as described above. These flasks were shaken in incubators at 37 °C for 24 hours, and the OD600 values were measured using Ultraspec 10 Cell Density Meter (Amersham Biosciences). For western blot analysis, cells were prepared as for growth rate measurements, and collected at OD600 = 0.6.

Western blot analysis

Anti-MinD crude serum⁴, a kind gift from Lawrence Rothfield was affinity purified using His-MinD proteins, a kind gift from Yaron Caspi, to enhance the specificity. FtsZ polyclonal antibody (affinity purified, Acris Antibodies) was used to quantify the amount of FtsZ in the protein sample, serving as a control for the total protein level loaded onto the lanes. Four strains, W3110, FW1363, FW1555, and FW1590 were inoculated in M9 medium supplemented with glucose and PHA overnight, back diluted to OD600 = 0.02 in 100 ml fresh medium (as above) and incubated under the same condition. Cells were collected at OD600 = 0.6, and centrifuged at 4 °C for 20 minutes at 4000 rpm. Supernatants were disposed and cells were collected and lysed using B-Per Reagent (Thermo Scientific) for total cell extract. The protein concentrations were determined by Bradford analysis, using series-dilutions of BSA as calibration standard. 10 µg protein content from each sample was loaded onto 10% Bis-Tris gel (NuPage Invitrogen). The protein was blotted onto PVDF membrane (0.2 µm Pore Size Novex, Invitrogen), blocked, and washed, and then incubated at 4 °C with affinity-purified MinD antibody. The second antibody used was goat-anti-rabbit antibody conjugated with horseradish peroxidase (Jackson Imm. Research), which is detected by incubation in Chemiluminescent substrate (Thermo Scientific) and exposure in Biorad Chemidoc XRS+. The image was background subtracted and the intensities of the protein bands were quantified using ImageJ Software (Supplementary Fig. 3). The membrane was briefly incubated in 0.2M Glycin-HCl buffer to strip away the MinD antibody, washed with TBS-T buffer, re-blocked with milk and used for the immune blotting of FtsZ.

Image analysis

Analysis of fluorescent microscopy images was carried out using Matlab. The boundary of a cell was determined based on the cytosolic eqFP670 images. For cell morphology measurements of the rod-shape *E. coli*, we used the DipImage Toolbox (<http://www.diplib.org>). Briefly, a fluorescent image was Gaussian-blurred to be used for background subtraction, and a threshold was applied to transform the background-subtracted image into a binary image. The cells were individually identified by DipImage toolbox and the Feret values, including maximum Feret diameters (lengths) and minimum Feret diameters (widths) were measured and used for statistical analysis (Supplementary Fig. 3e-h). For cells shaped by micro-chambers, the cytosolic fluorescence image of each single cell was manually isolated from the full fields of view for processing. Background was subtracted as described above to produce binary images for extraction of the contour line. The smallest rectangle that contains the cell was used to define cell length, width, and relative occupancy of the cell in the rectangle (Supplementary Fig. 7a-d).

For oscillation angle measurements, an SD image of the sfGFP-MinD image was background subtracted, Gaussian filtered, and transformed into binary image. The polar zones were detected through morphological operations provided by the Image Processing Toolbox of Matlab. The oscillation angles were determined by the lines connecting the centers of the detected polar zones, i.e.

the mean coordinates of all pixels within the polar zone (Supplementary Fig. 7a-d). The measured oscillation angle was used to select for the axis for measuring the intensity profiles, which is then concatenated into kymographs of the time series. At each time point, we used the line profile to determine the peak position and peak intensity of the polar zones, from which we determine the polar residence time and oscillation period (Supplementary Fig. 8). The oscillation angles of stripe patterns were the mean of angles measured between individual polar zones and the middle stripe. The polar residence is defined by the time span between the appearance and disappearance of a peak within a polar zone. The period of oscillation is defined as the time between two peaks of the same polar zone in the peak intensity plot.

Diversity index

The diversity index is measured using Shannon entropy⁵ using the following equation:

$$H = -\sum_{i=1}^N p_i \ln p_i$$

Here N is number of modes present in one cell size, and p_i is the fraction of this mode.

Numerical simulation

The computational model takes into account the minimum set of interactions that are essential to reproduce the pole-to-pole oscillations in rod shape bacteria^{6,7}:

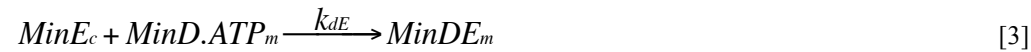
1) Membrane binding of cytosolic MinD in its ATP-bound form (MinD.ATP_c).



2) Recruitment of cytosolic MinD.ATP_c by membrane-bound MinD.ATP_m.



3) Binding of cytosolic MinE (MinE_c) to the MinD.ATP_m to form a MinDE complex (MinDE_m) on the membrane



4) ATP hydrolysis of MinD, which leads to the dissociation of the MinD and MinE from each other and from the membrane



5) Nucleotide exchange of cytosolic MinD



Equations (1) – (5) were used to construct a reaction diagram within a cytosolic compartment and the cytoplasmic membrane space that fully encloses the cytosol, using the software package VirtualCell (<http://vcell.org>). Note that parameters are converted to adapt to the unit system for deterministic simulations in VCell.

The equations describing the time evolutions of the MinD and MinE concentrations arising from the listed interactions are:

$$\frac{\partial}{\partial t} c_{DD} = D_{DD} \nabla^2 c_{DD} - \lambda c_{DD} + \delta(S)(k_{de} c_{de}) \quad [6]$$

$$\frac{\partial}{\partial t} c_{DT} = D_{DT} \nabla^2 c_{DT} + \lambda c_{DD} - \delta(S)(k_D c_{DT} + k_{dD} c_d c_D) \quad [7]$$

$$\frac{\partial}{\partial t} c_E = D_E \nabla^2 c_E + \delta(S)(k_{de} c_{de} + k_{dE} c_d c_E) \quad [8]$$

$$\frac{\partial}{\partial t} c_d = D_d \nabla_m^2 c_d + \delta(S)(k_D c_{DT} + k_{dD} c_d c_{DT} - k_{dE} c_d c_E) \quad [9]$$

$$\frac{\partial}{\partial t} c_{de} = D_{de} \nabla_m^2 c_{de} + \delta(S)(k_{dE} c_d c_E - k_{de} c_{de}) \quad [10]$$

Here, c_{DD} , c_{DT} , c_E , c_d , and c_{de} denote the local concentrations of MinD.ADP_c, MinD.ATP_c, MinE_c, MinD.ATP_m, and MinDE_m, respectively. $\delta(S)$ is a delta function that restricts the reactions that only occur at the boundary of the compartment.

The parameter screening was initiated from the set of the parameters in the Halatek-Frey model⁷. The final set of reaction kinetic parameters used to reproduce symmetry selection, gradient scaling, and all the major patterns are listed in Table S4. The MinD/MinE concentration ratio and diffusion rates are set to be identical with the simulations in the Halatek-Frey model, where the choices of these values are explained. Based on the set of interactions and kinetic parameters, a reaction diagram was constructed of reactions occurring within a membrane-coated cytosolic compartment, using the software package VirtualCell. Three-dimensional compartments were constructed and latticed with a grid spacing of $dx = dy = dz = 0.08 \mu\text{m}$. The height of all objects was fixed to be $z = 1.00 \mu\text{m}$.

The numerical integration of the partial differential equations was carried out over time in VirtualCell using a ‘fully implicit, adaptive-time-step finite-volume method’, which employs the sundials stiff solver CVODE for time stepping. The results of the deterministic solutions in the three-dimensional compartments were exported in the form of Nearly Raw Raster Data (.nrrd) files for volume data and Unstructured Cell Data (.ucd) files for membrane data. These data were then integrated and projected onto a two-dimensional plane by a customized Matlab script.

The resulting images were used to display the final oscillation patterns and to measure oscillation angles (Fig. 4). All simulation results in the figures show the sum of MinD molecules in all forms, i.e., including MinD.ADP_c, MinD.ATP_c, MinD.ATP_m, and MinDE_m. Because the exact values at the boundary of the rectangles in a 2-dimensional projection strongly depend on the lattice size, we use the following formula for the 2-dimensional projection of the molecular concentration data exported from the lattices in the 3-dimensional simulations for convenience in displaying the results:

$$u_{DD} = \int_0^1 (u_{DD} + u_{DT}) dz - 2(u_d + u_{de}) \quad [11]$$

Here, u_{DD} and u_{DT} respectively represent the concentrations of MinD.ADP_c and MinD.ATP_c in a lattice, and u_d and u_{de} stand for the mean concentration of MinD.ATP_m and MinDE_m, respectively, along the z axis. As shown in equation (11), the concentrations at the boundary lattices of the 2D projection are computed by taking the mean of the concentration along the z -axis and multiplying by two to account for the upper and lower membrane. The values at the boundary pixels of the 2 dimensional rectangles are slightly underestimated due to the higher amount of membrane at the boundaries that allows MinD binding.

For screening of kinetic parameters, non-homogeneous initial concentrations of MinD and/or MinE were set to explore the different modes of oscillations. For probing the minimum width for transversal oscillations in our model, MinD molecules were initially all located in half of the cytosolic volume in its ATP-bound form with a boundary line perpendicular to the cell width, whereas MinE was homogeneously distributed in the cytosol of the $10 \mu\text{m}$ long cells. For testing the symmetry-axis alignment in relation to aspect ratio, MinD molecules were initially concentrated at one corner of rectangular cells with a fixed width of $2 \mu\text{m}$ and lengths between 2 and $3.5 \mu\text{m}$ (Supplementary Fig. 7), whereas the MinE molecules were initially concentrated at the other diagonal corner. For recapturing the oscillation modes in the full rectangular grid (Fig. 5e), the simulations initiated with the concentration gradients (cytosolic MinD) shown in Supplementary Movie 9. For square shapes, MinE was initially distributed homogeneously in the left half of the cytosol, whereas for all other rectangular shapes MinE was initially distributed homogeneously in the whole cytosol.

Supplementary Discussion

MinD-binding to internalized, positively curved membranes

Here, we show that the incidences of MinD binding to positively curved membranes (of internalized vesicles which we sometimes observe, especially for large cell volumes) do not affect the Min oscillations by either curvature⁹ or mechanical interactions⁸.

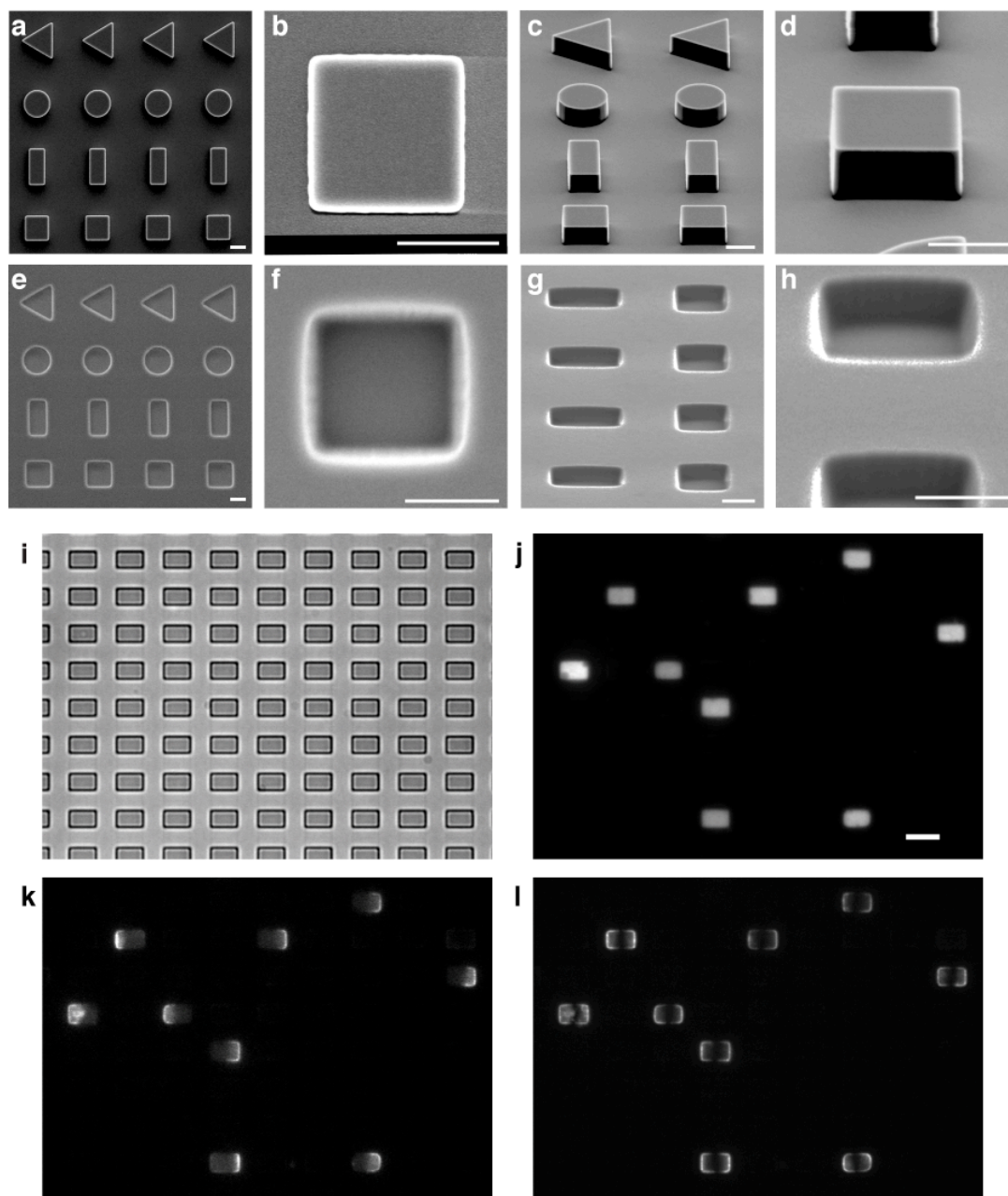
As cells can grow to remarkably large sizes under the treatment of A22 and cephalixin, their surface-to-volume ratios decrease. This has been shown to induce invagination of the excessive cytoplasmic membrane due to the fact that the amount of phospholipids in the cells is synthesized to be in scale with the cell volume⁸. A previous study reported that such an effect can lead to the localization of the MinD and FtsZ to the internalized membrane, thus impeding cell division⁸. In our study, the cells had a fixed height due to their growth constraint in the vertical direction, since the depths of the chambers were kept at 1.15 μm . As a result, the surface-to-volume ratios of these cells are larger than spherical cells, but smaller than the wild-type rod-shapes. The internalized membranes are mainly observed in cells with sizes larger than 20 μm^3 , e.g. in squares larger than 4.5 x 4.5 x 1 μm^3 (Fig. 2a). Despite the fact that sfGFP-MinD frequently localize to the internalized membranes (Fig. 3a), the global direction of the Min oscillation is found not to be affected by these binding events. The locations of sfGFP-MinD that bind to internalized membrane stay truthful to the rules derived in this study, and the same oscillation patterns are found for cells with and without internalized vesicles.

Together with the fact that Min oscillations prefer the side-to-side orientations rather than a direction among the more curved diagonal corners, the ability of sfGFP-MinD to bind positively curved membrane demonstrates that negative membrane curvature *per se* does not dictate the orientations of the Min oscillations. Furthermore, the binding of sfGFP-MinD to these randomly located excessive membranes does not affect the dynamics and orientations of the Min oscillation, indicating the robustness of global Min oscillations against small perturbations of local membrane topology.

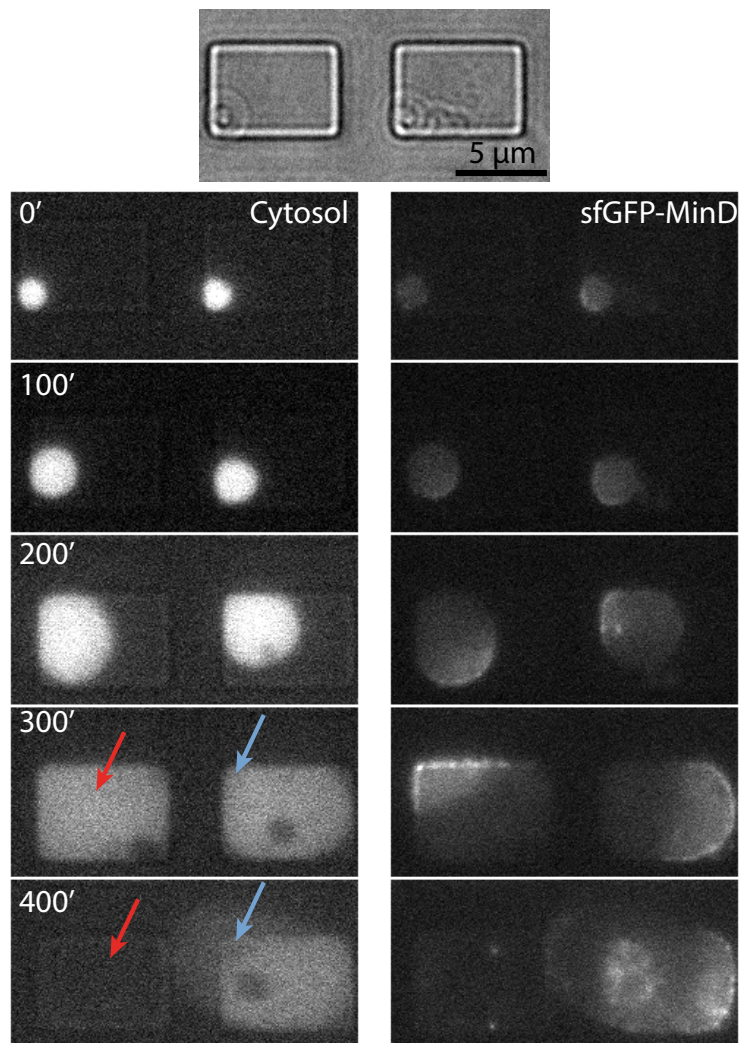
Binding of sfGFP-MinD to the internalized membrane vesicles did not induce shrinking or tube formation of the latter. These observations are thus different from the vesicle shrinking and tube formation observed *in vitro* by high concentrations of MinD and/or MinE^{9,10}. In this case, the *in vivo* oscillations do not generate forces that alter the mechanical properties of the membrane dramatically.

The observation of amoeba-shaped MinD patches in *in vitro* experiments on lipid surfaces has led to an alternative hypothesis that attribute the Min dynamics to a characteristic MinD-binding area arising from mechanical interactions between MinD/MinE oligomers¹¹. We do not observe such effects *in vivo*: 1) the transitions between longitudinal pole-to-pole and stripe patterns largely depend on the cell length, rather than on the amount of membrane (Fig. 2, Fig. 3). 2) Binding of Min proteins to internalized membrane vesicles with various sizes does not alter the patterns of the global Min oscillations.

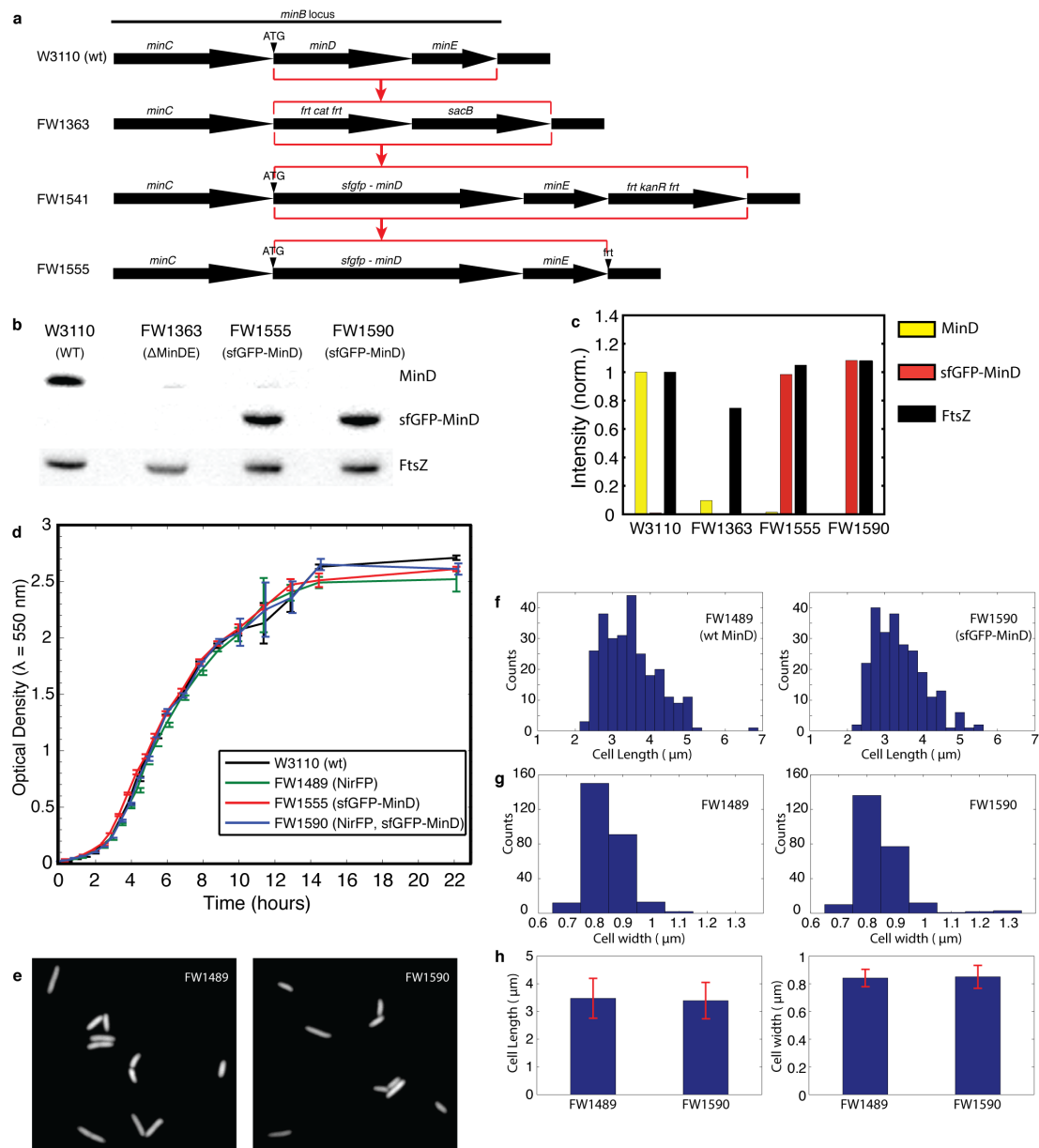
Supplementary figures



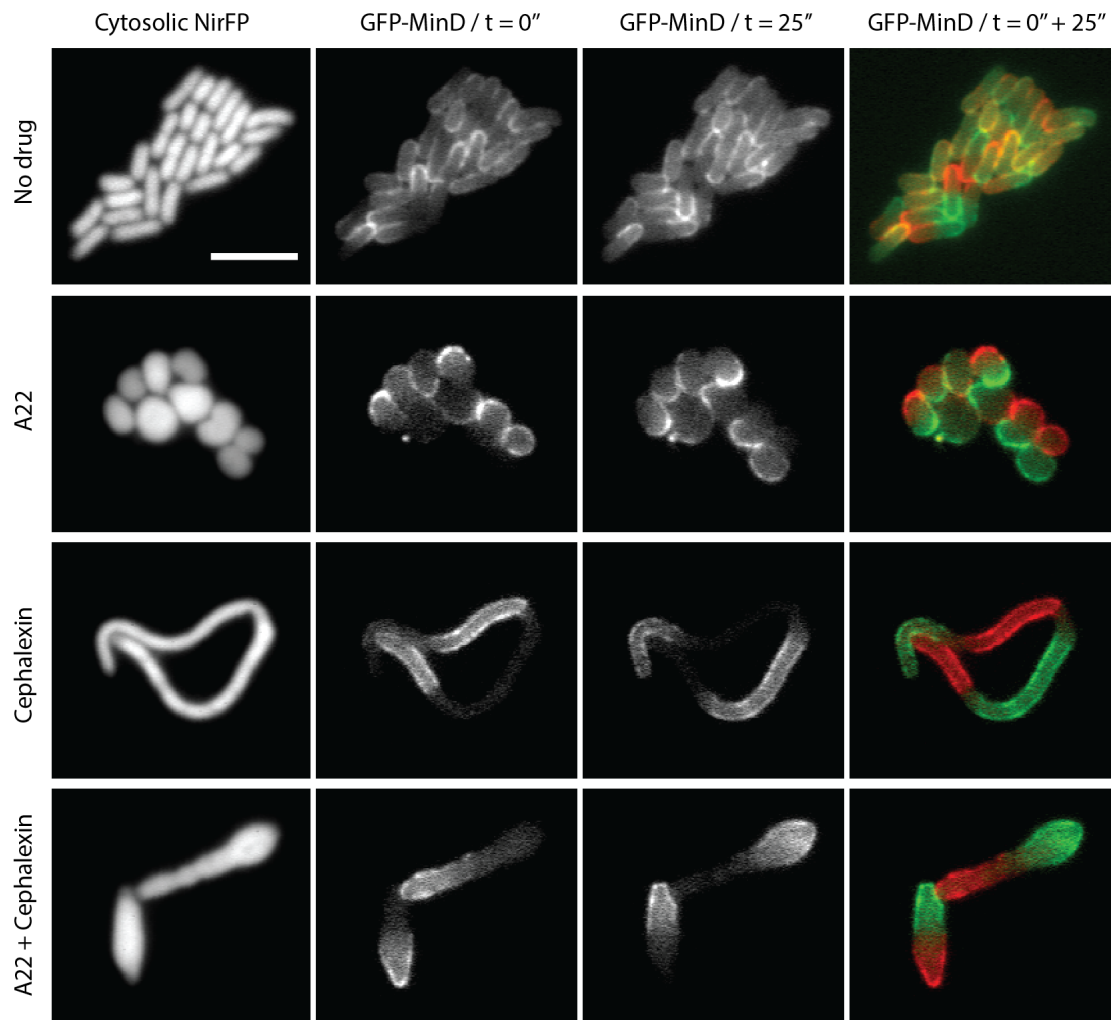
Supplementary Fig. 1. Scanning electron microscopy (SEM) images of microstructures and optical microscopy images of a typical field of view during a cell-sculpting experiment. a – d, SEM images of nanofabricated silicon structures at different magnifications. **e – h,** SEM images of PDMS chambers at different magnifications. **a, b, e, and f** are top views. **c, d, g, and h** are imaged at a 45 ° angle. **i,** Bright field optical image of an array of rectangular PDMS chambers with sizes of approximately 4 μm x 2.5 μm x 1 μm , which was used for cell-sculpting. **j,** Cytosolic eqFP670 signal of cells grown into the shapes of the PDMS chambers, which have the same size as shown in **i**. **k,** sfGFP-MinD fluorescence at one time point. **l,** Standard-deviation image of sfGFP-MinD over 25 frames taken every 5 seconds. Bars in a-h are 2 μm , and bar in j is 5 μm .



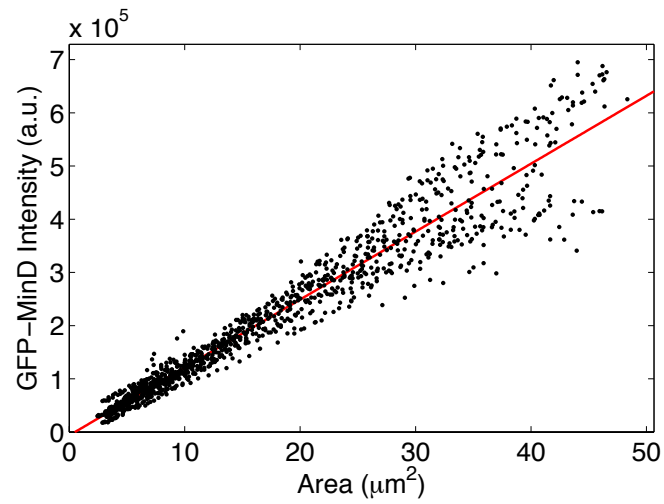
Supplementary Fig. 2. Growth of the cells into large sizes. The red arrows indicate that the left cell ruptured after fully filling the chamber, while the blue arrows indicate that the right cell grew out of the chamber. The time labels are in minutes.



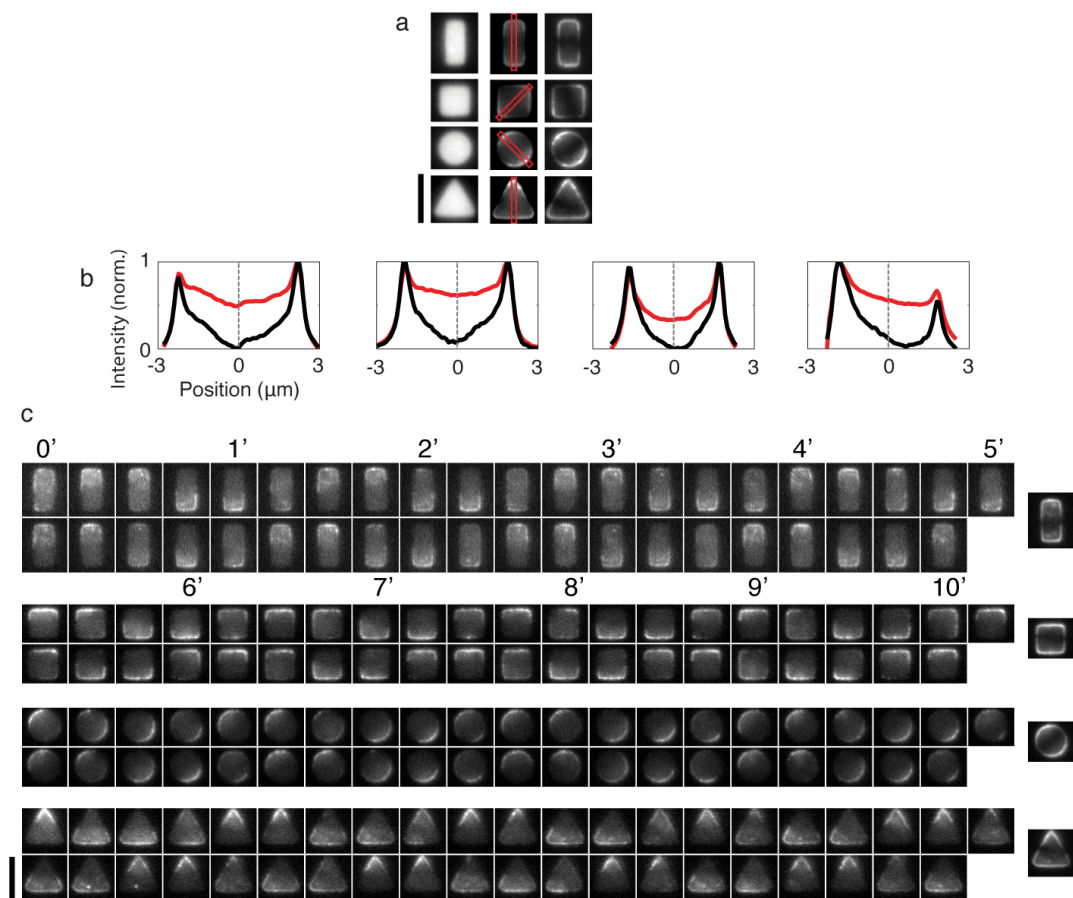
Supplementary Fig. 3. Genomic insertion of *sfgfp-minD* fusion retains the wild-type protein expression level, cell growth rate and cell morphology. **a**, Schematic of the *minDE* knockout and insertion of *sfgfp-minD* fusion gene at the endogenous *minB* locus. Note that the wild-type promoters and ribosome-binding sites of MinD and MinE are all left intact in the final construct *sfgfp-MinD::minE*. Bacterial strain names are on the left. ATG is the start codon. Frt stands for flippase recognition target site. **b**, Western-blot results showing the expression level of MinD and sfGFP-MinD in various strains using anti-MinD antibody, and that of FtsZ using anti-FtsZ antibody. **c**, Bar plot showing the expression level of MinD (yellow), sfGFP-MinD (red) and FtsZ (black, control) quantified from B. The MinD and sfGFP-MinD levels were normalized against MinD expression in W3110 wildtype, whereas FtsZ is normalized against FtsZ expression in W3110 wildtype. The plot shows that the sfGFP-MinD/FtsZ ratio in the final strain FW1590 is almost identical to the MinD/FtsZ ratio in wild-type. **d**, Growth curves of the strains grown at 37 °C in M9 medium supplemented with glucose and protein hydrolysate ampicase. Error bars are standard deviation. **e**, Cytosolic fluorescence images of the cells from liquid culture growing at exponential phase. **f**, Histograms of cell length distribution in these cells. **g**, Histogram of cell width distribution in these cells. Error bars are SD. Total cell counts are 268 for FW1489 and 241 for FW1590. Note that the lengths and widths are Feret lengths and widths.



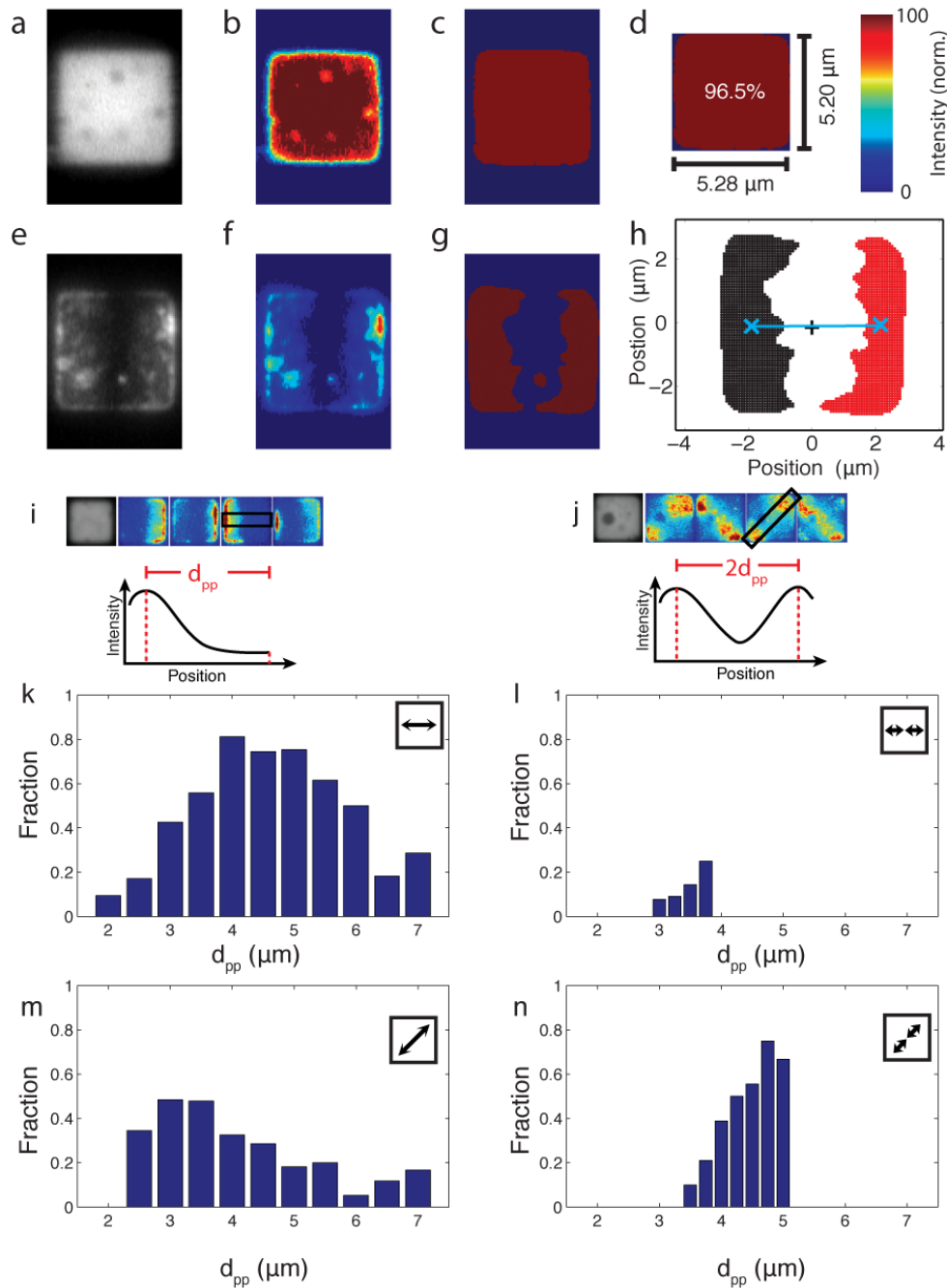
Supplementary Fig. 4. Modes of growth and sfGFP-MinD localization in cells under different drug treatments. These cells are imaged after 3.5 - 4 hours of growth at 26 °C under an agarose pad containing 1.5% agarose, M9 medium supplemented with glucose and protein hydrolysate ampicase, and drugs as indicated at the left of the images. The concentrations of the supplements are as indicated in the SOM methods. Bar is 5 μ m.



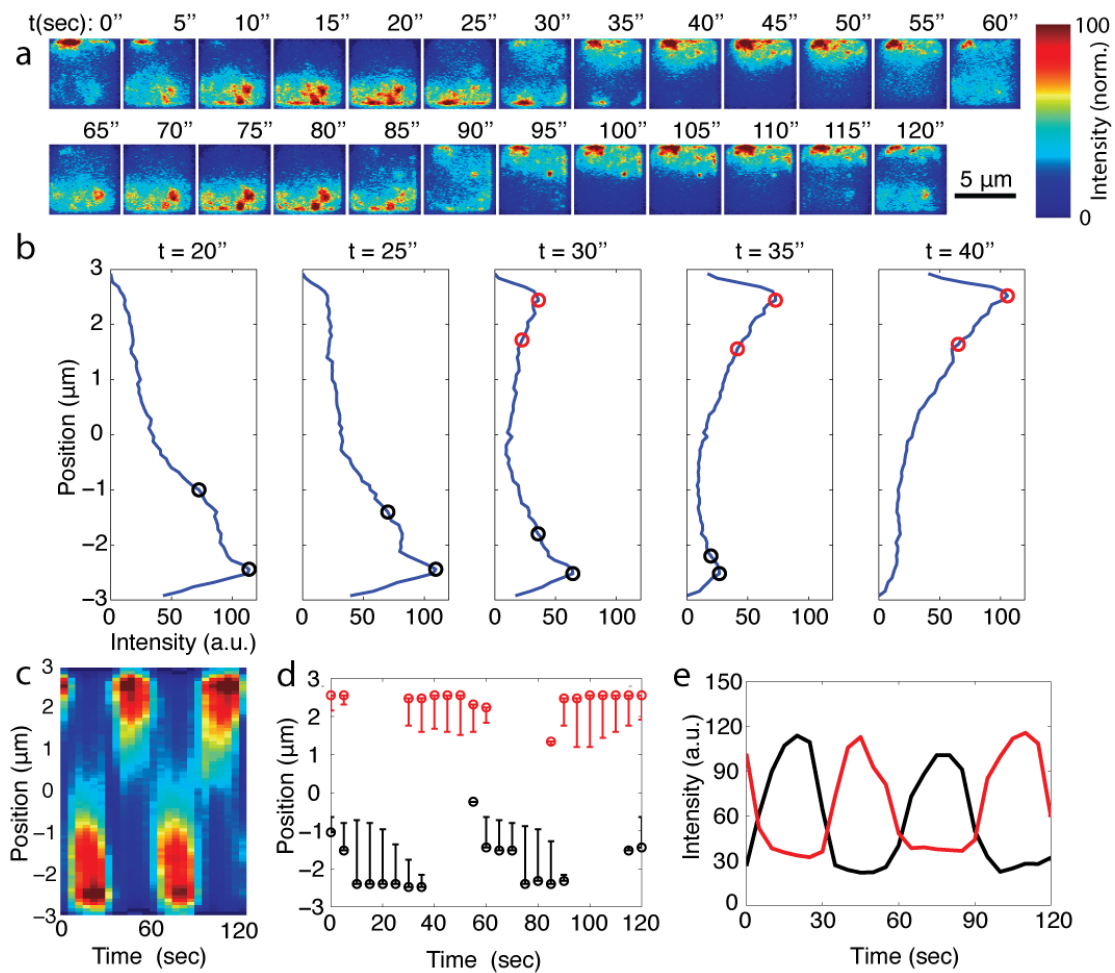
Supplementary Fig. 5. Total sfGFP-MinD intensity in cells of different area size measured in micro-chambers. The MinD fluorescence is found to scale linearly with cell volume, i.e., the MinD concentration is constant. Red line is a linear fit on the data ($R^2=0.935$). The number of data points is 1152.



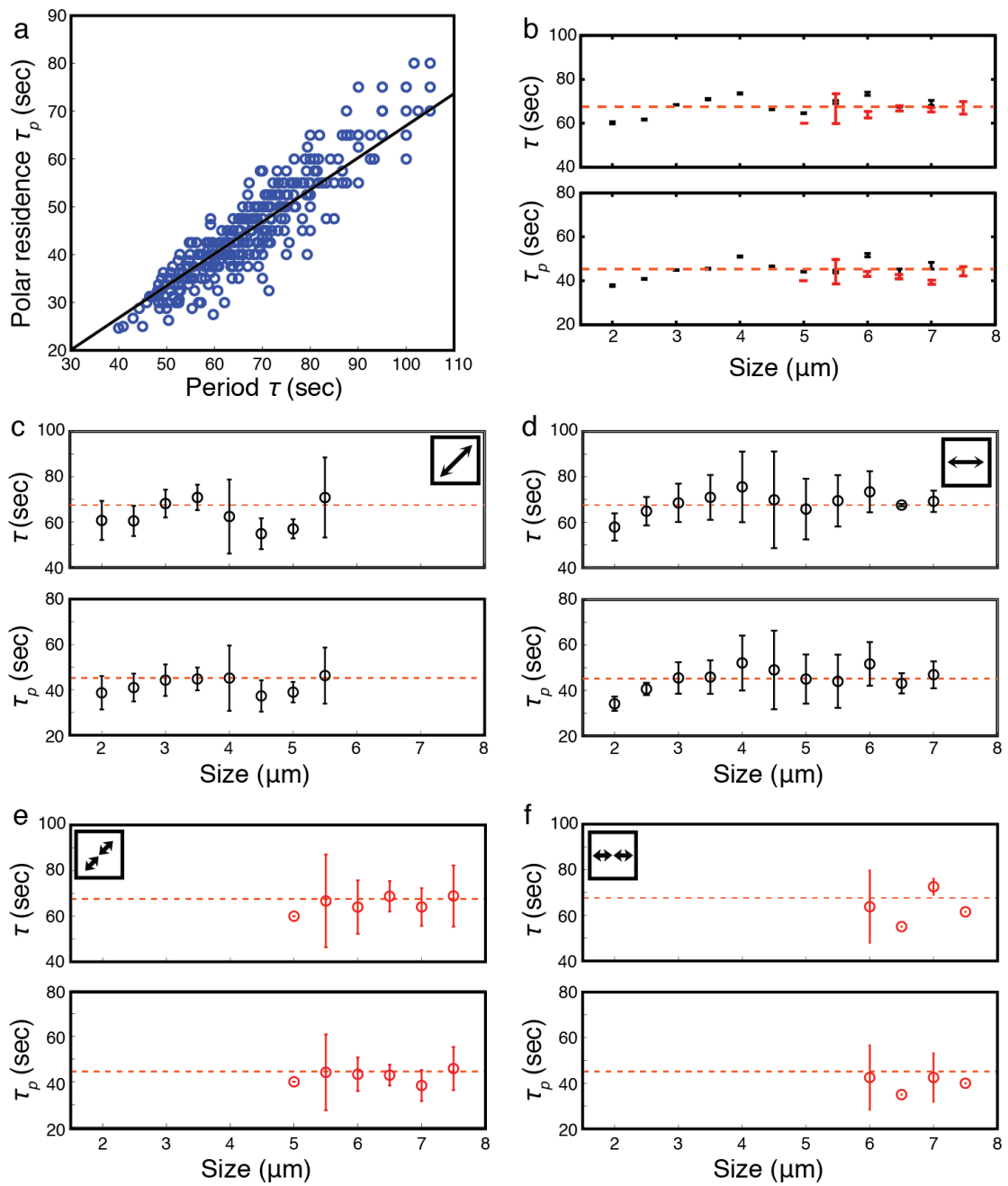
Supplementary Fig. 6. Concentration profiles and long-term MinD dynamics in diverse shapes. a, From left to right, cytosol imaged, mean and SD of sfGFP-MinD signal in shaped cells. **b,** Intensity profiles along the length of the red-rectangle region in **a**. Red and black show the time-averaged intensity and SD of the same region, respectively. **c,** sfGFP-MinD fluorescence signals that oscillate in 4 shapes over a 10-minute period. Frame rates are 15 seconds. The right side shows the standard-deviation (SD) images. Oscillations follow the symmetry axes, but show deviations due to intrinsic stochasticity and extrinsic noise in the cellular environment. All time labels are in minutes.



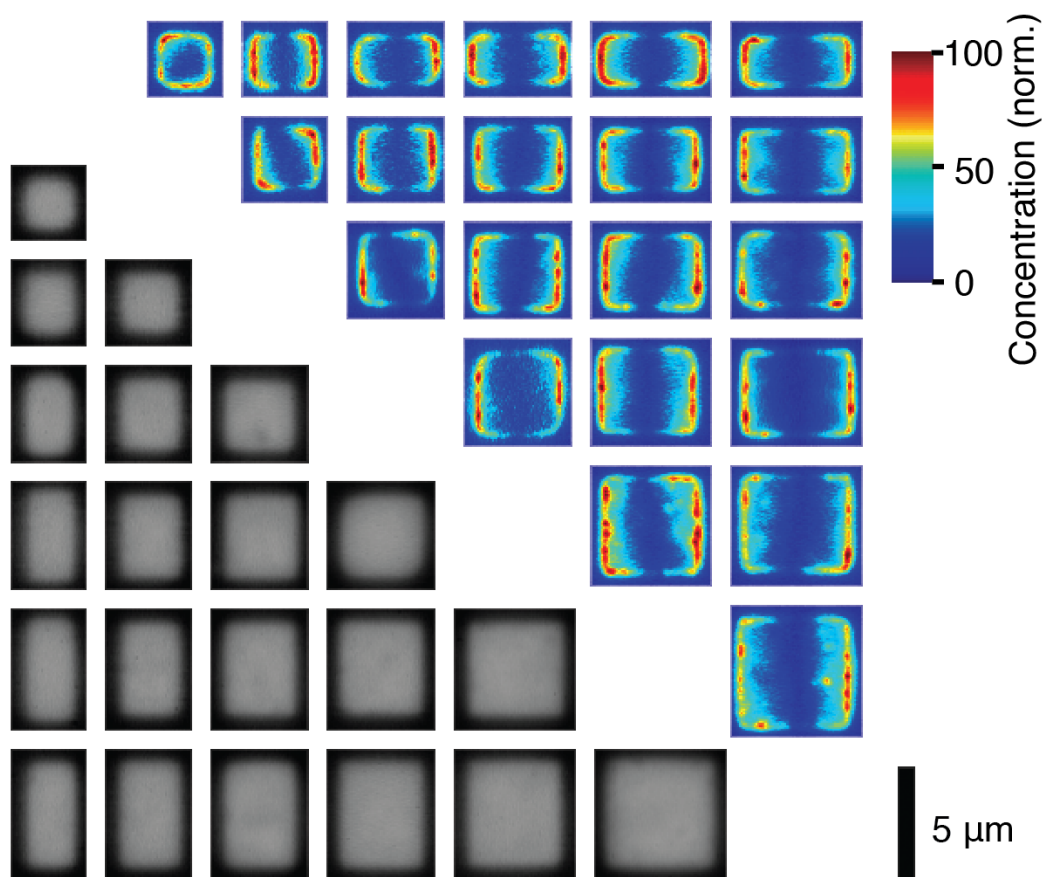
Supplementary Fig. 7. Image analyses for determining cell dimensions, Min oscillation angles and pole-to-pole distances. **a**, Grey scale fluorescence image showing the cytosolic eFP670 signal. **b**, image in **a** after background subtraction, shown in heatmap. **c**, A binary image of cytosol obtained after a threshold was applied to the image of **b**. **d**, The occupancy of the cell in the smallest fitting rectangle. Numbers in the middle show calculated occupancy. **e**, SD of sfGFP-MinD signal computed per-pixel. **f**, Data of **e** after background subtraction and Gaussian blurring, shown in heatmap. **g**, A binary image obtained after a threshold was applied in **f**. **h**, A plot of two distinguished polar zones, which were detected by morphological operations in Matlab. The two individual polar zones are shown in black and red, respectively. The center of mass of the cell is marked by black '+'; the centers of the polar zones are marked by blue crosses and connected by a line. **i**, **j**, Two examples showing pole-to-pole oscillations and stripe oscillations, respectively, with illustrations how pole-to-pole distances (d_{pp}) are defined in these two patterns. **k-n**, bar plots showing the distribution of d_{pp} occurring at each oscillation mode.



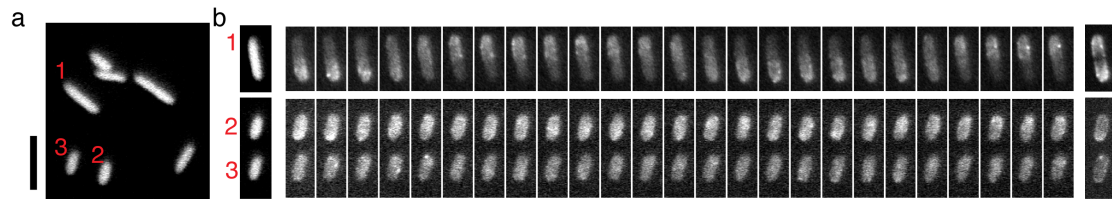
Supplementary Fig. 8. Temporal dynamics of sfGFP-MinD in a square-shaped cell. **a**, The time-lapse image of sfGFP-MinD in the same cell as in Supplementary Fig. 7, rotated 90° counterclockwise. **b**, Mean intensity plots along the oscillation direction at 5 time points. Each data point is the mean intensity value perpendicular to the oscillation direction. Circles indicate the peak and the full-width-at-half-maximum (FWHM) at one side. Red and black represent two polar zones as in Supplementary Fig. 7h. **c**, Kymograph showing the mean sfGFP-MinD intensity over time. Values are calculated as in b, but now plotted as a heatmap. **d**, Polar-zone peak (circle) positions and FWHM (bar) positions plotted over time, measured as in b and used for calculating polar residence time (τ_p). **e**, The peak intensity value of polar zones plotted over time. This is used to calculate the oscillation period (τ).



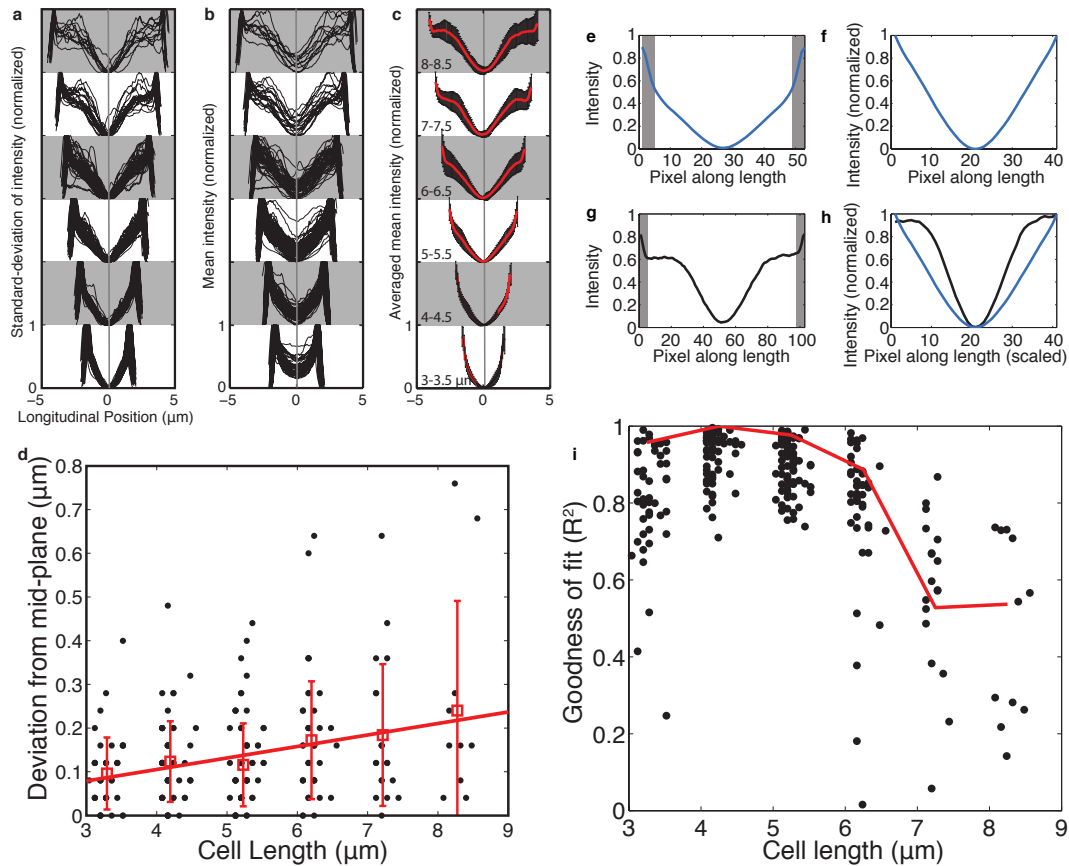
Supplementary Fig. 9. Polar residence time (τ_p) and oscillation periods (τ) in the square-shape cells. **a**, Scatter plot of polar residence time against oscillation periods in all cells. The black line is a linear fit $\tau_p = 0.67 * \tau$ ($R^2 = 0.84$), indicating that the mean value of the τ_p/τ ratio is 0.67. **b**, τ and τ_p in relation to cell sizes; error bars are standard error of the mean (SEM). **c-f**, τ and τ_p in different modes of oscillations; error bars are standard deviations. In **b – f**, black data points represents the pole-to-pole oscillation, red data points represents the stripe patterns, and the red dash line represents the mean value of τ and τ_p for all cell sizes.



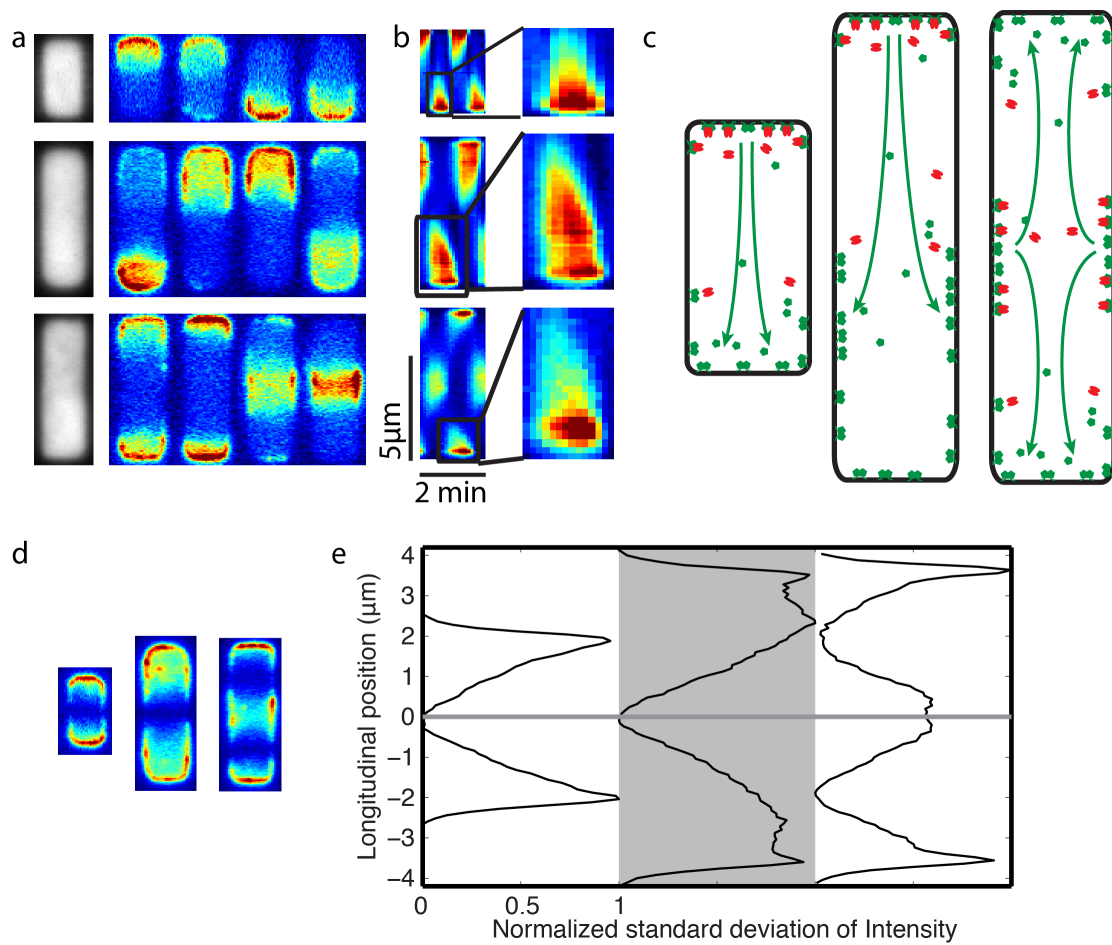
Supplementary Fig. 10. Min oscillations in rectangular and square shapes with sides between 2 and 4.5 μm . Bottom left grid is the cytosolic eqFP670 signal; top right grid is the SD of the Min signal in the same cells in correspondence to the bottom left grid. For the cytosolic images, the cell length difference between rows are $\sim 0.5 \mu\text{m}$; the width difference between columns are $\sim 0.5 \mu\text{m}$.



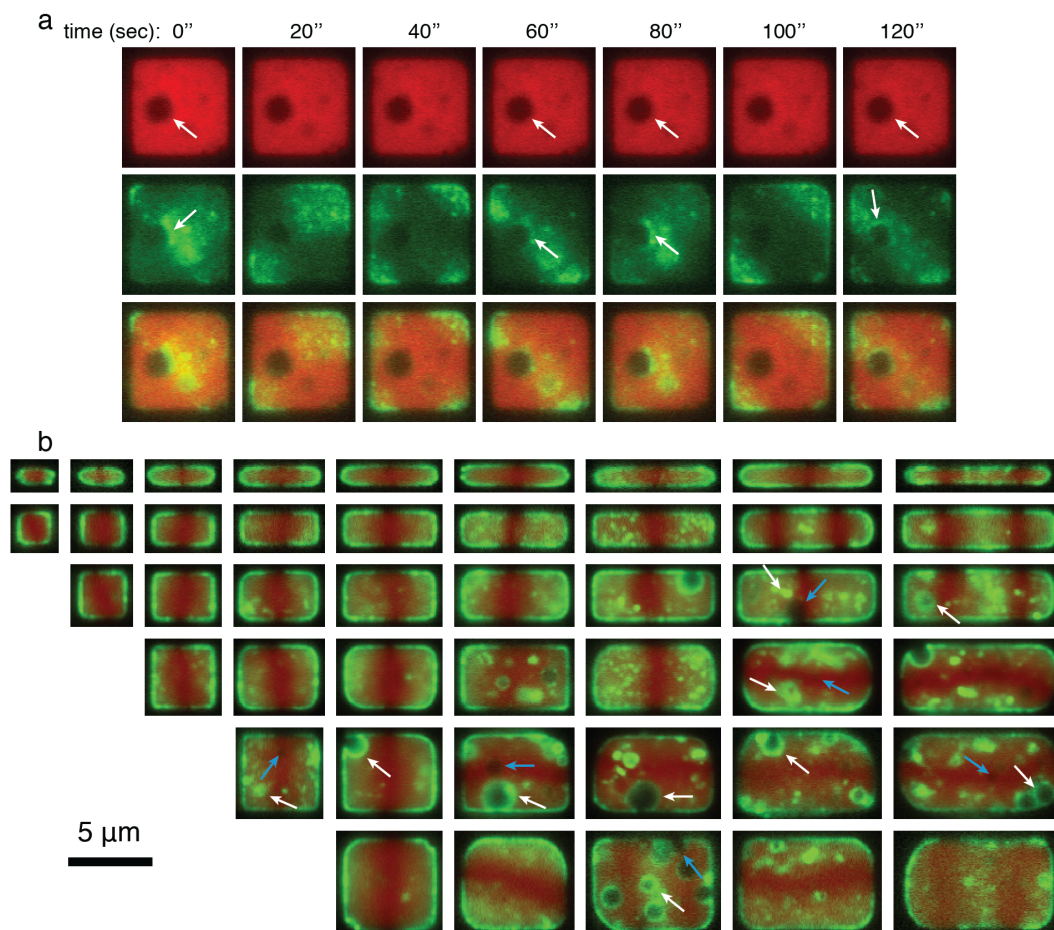
Supplementary Fig. 11. Rod-shape cells below 2.5 μm do not show consistent oscillations **a.** Exponentially growing cells from the same culture placed on a glass cover slip. **b.** 3 cells are cropped from a to show the sfGFP-MinD dynamics. Shown are a cytosolic image, time-lapse images of sfGFP-MinD, and SD images. Cell lengths are, from top to bottom, 4.1 μm , 2.4 μm and 2.3 μm . Scale bar, 5 μm .



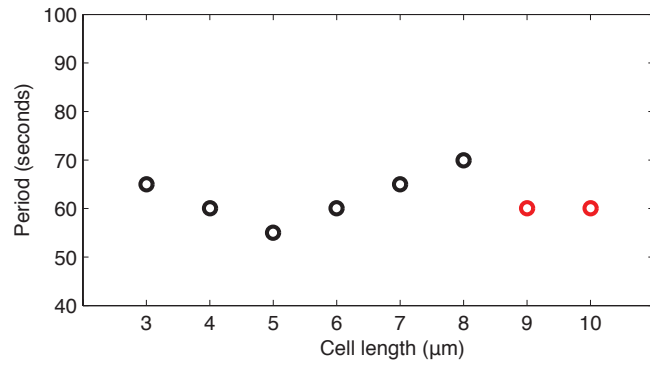
Supplementary Fig. 12. Mid-plane definition and gradient scaling of Min patterns in relation to cell length. **a**, sfGFP-MinD SD profiles and **b**, mean (time-averaged) intensity profiles along the long axes in individual rectangular cells (widths between 2 and 3.5 μm). **c**, Averaged mean intensity in each size group calculated after scaling each single profile in **b** against central minima and polar maxima. **d**, Deviation of the SD profile minimum from the center of the cell lengths in relation to cell length. Dots show individual cells (note that there are overlapping data points). Boxes and error bars are mean and standard deviation values, fitted by a red line, which indicates that the mean deviation is around 2.6% of the cell length across cell lengths between 3 and 8.5 μm . **e-h**, Illustrations of sfGFP-MinD SD profiles (**e,g**) with tails cropped to eliminate the high intensity due to high cell membranes content at the cell poles, and how they are scaled to compare the SD profiles in different cell sizes (**f,h**). **i**, Scaling effect in relation to cell size. Black dots show the goodness of fit of scaled individual SD profiles against the averaged SD profile of 4-4.5 μm cells shown in **f**. Red line connects the goodness of fit of the averaged profile in each size group against the averaged profile of 4-4.5 μm cells.



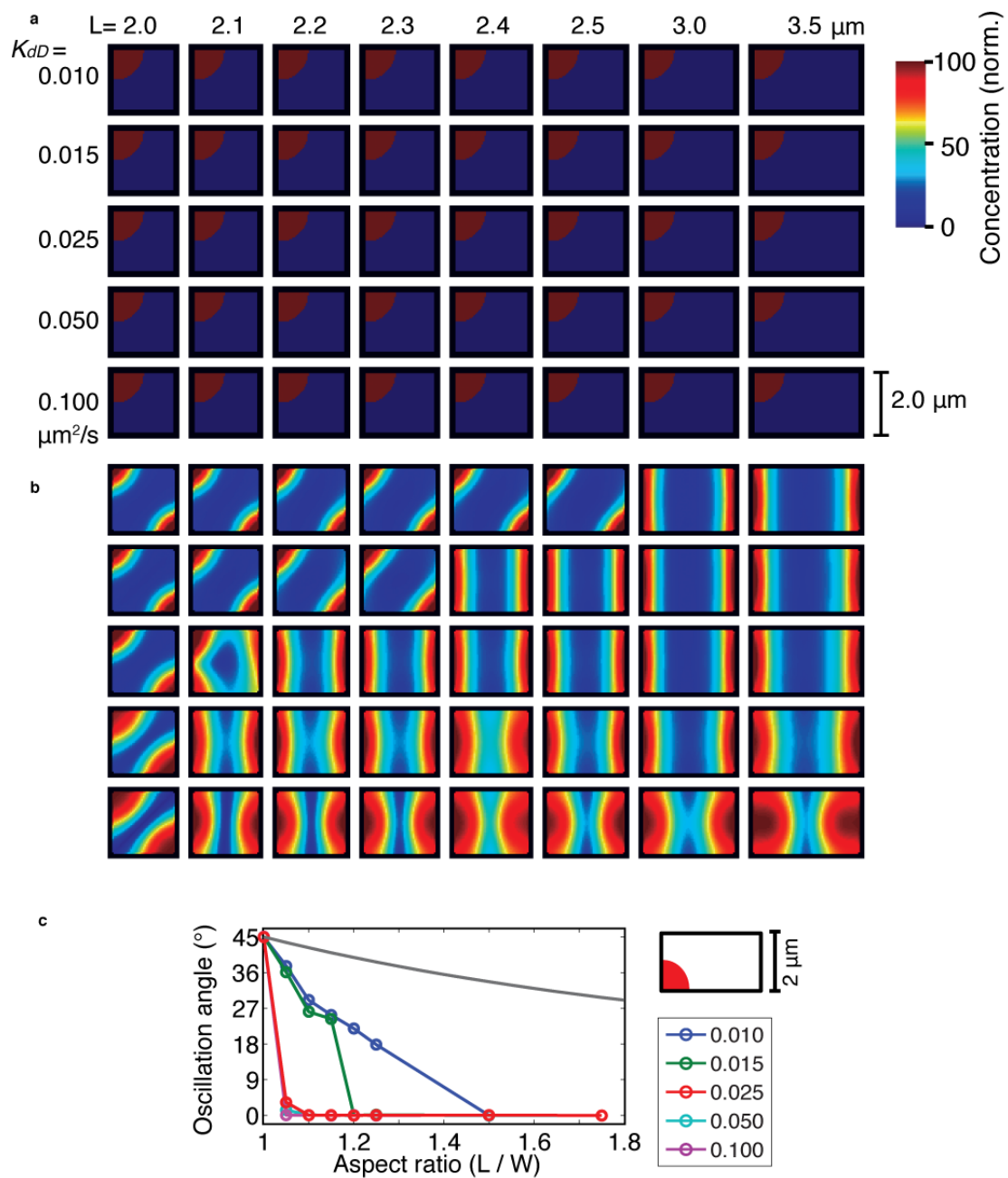
Supplementary Fig. 13. Comparing sfGFP-MinD dynamics in different cell lengths. **a**, sfGFP-MinD dynamics in 3 cells with different lengths. From left to right: cytosolic image, time-lapse images shown in heat plot with time-interval of 15 seconds. **b**, kymograph of sfGFP-MinD intensity along cell length. One of the polar zones in each panel was magnified to show progression over-time. **c**, Illustrations of MinDE dynamics in different lengths and oscillation modes shown in a. Green is MinD, red is MinE. **d**, SD images of sfGFP-MinD in cells shown in a. **e**, Intensity profiles of the SD images along the long axes of the cells shown in d.



Supplementary Fig. 14. The binding of sfGFP-MinD to the internalized membrane is determined by the locations of the membrane but not its curvature, and it does not induce tube formation or shrinking of the membrane. a, Time-lapse images of cytosolic eqFP670 fluorescence (red) and sfGFP-MinD oscillations (green) in a cell containing visible vesicles, shown in false color. Red is cytosolic eqFP670; green is the sfGFP-MinD. **b**, False-color overlay of cytosolic eqFP670 and the SD images of sfGFP in rectangular cells. **a** and **b**, White arrows indicate positively curved membrane bound by sfGFP-MinD; cyan arrows indicate positively curved membrane not bound by sfGFP-MinD.



Supplementary Fig. 15. Period of the Min oscillations in rectangular cells with a width of 2 μm determined from numerical simulations. Black circles, pole-to-pole oscillations; red circles, stripe oscillations. The temporal resolution of the measurement is 5 seconds, set by the frequency of the data recording during simulations.



Supplementary Fig. 16. Increasing MinD recruitment rate (k_{dD}) enhances the alignment of oscillations to the symmetry axis in rectangular cells with a width of 2 μm . **a**, 2-dimensional projections of the initial MinD distribution ($t=0''$) provided for numerical simulations with given shapes and parameters. **b**, SD images of the 2D projection of the simulation results at between $t=480''$ and $t=600''$ in simulations. **c**, Final oscillations angles in relation to aspect ratio. Initial MinD localization depicted at the top right corner. Different colors show results from different k_{dD} values.

Supplementary tables:

Table 1. Number of cells selected for the quantification in each size category

width/ length (μm)	0.75 1.25	1.75 2.25	2.25 2.75	2.75 3.25	3.25 3.75	3.75 4.25	4.25 4.75	4.75 5.25	5.25 5.75	5.75 6.25	6.25 6.75	6.75 7.75
1.75- 2.25	-	47										
2.25- 2.75	9	36	33									
2.75- 3.25	117	6	40	51								
3.25- 3.75	87	18	34	34	34							
3.75- 4.25	78	12	31	23	23	76						
4.25- 4.75	45	14	6	12	6	23	49					
4.75- 5.25	42	77		40		39		100				
5.25- 5.75	36											
5.75- 6.25	26	54		30		52		23		41		
6.25- 6.75	32											
6.75- 7.25	29	34		20		36		34		44		12
7.25- 7.75	25											
7.75- 8.25	18	65		20		17		42		14		
8.25- 8.75	27											
8.75- 9.25	14	31		39		10		43		16		
9.25- 9.75	19											
9.75- 10.25	16	30		33		25		12		18		
10.25- 10.75	13											

Table 2. Primers

Name	Sequence (5'-3')
929	ggggacaactttgtatagaaaagttgcaactcaagggcatcggtcgagatcccgggtgcc
930	ggggacaagttgtacaaaaagcaggcttaatgagcagctgattaaggag
937	ggggacaagttgtacaaaaagcaggcttaatgggagaggatagcagctg
940	ggggacagcttctgtacaaagtgggtgtaggctggagctgcttc
944	ggggactgctttttgtacaaactggcatggtatatctccttctaaagttaaac
945	ggggaccactttgtacaagaaagctgggtatcaattaagcttggccccagtttgc
952	ggggaccactttgtacaagaaagctgggtatcagctgtgccccagtttgcctag
955	ggggacaactttgtataataaagttgcaattccggggatccgctgacc
1013	gcctgcgatatctggtgccgagccgcttgacggctagctcagtcctaggtacagtgc- tagctctagagaaaggagaaaactagatgagcagctgattaaggag
1020	cgaaaacaacaaggaaccgtgtgatcaattccggggatccgctgacc
1135	caaggcagagataactctgccttgaagataaatgcgctttfacagcgggctcaattccggggatccgctgacc
1206	gctttgaccgtcaaccgttaattgatcccttttaacaaggaatttctgtaggctggagctgcttcg
1207	caaggcagagataactctgccttgaagataaatgcgctttfacagcgggcatatgaatatcctccttag
1215	cgatgccggcagaatatagag
1238	cgtcgtaactacaacggtc
1239	tgagtcacttcatgcacc
1312	attccggggatccgctgacc
1326	ggggacaactttgtatagaaaagttgcatgaggtcacttcatgcaccag
1327	ggggactgctttttgtacaaactgacatctagtatttctcctcttc
1328	ggggacaactttgtataataaagttgacgtcgtaactacaacgggtcg
1410	ctctatattctgccggcatcg
1413	ggtcgacggatccccggaatgcgaacgtgaagcgaactgc
1471	ataaagaggagaaataactagatgcgtaaaggcgaagagct
1472	gatagaagagccagaaccgctttgtacagttcatccataccatg
1473	gctaccgctgccgctaccttcagcttctgcttccggaagg
1474	gctaccgctgccgctaccttcagcttctgcttccggaagg
1485	aaaacgctttgaccgtcaaccgttaattgatcccttttaacaaggaatttctatgcgtaaaggcgaagagctg

Table 3. Strains and plasmids

Strains	Descriptions	References
W3110	F-, lambda-, IN(rrnD-rrnE)1, rph-1	12 ¹²
FW1363	W3110, Δ <i>minD minE</i> :: <i>sacB cat</i>	This work
FW1541	W3110, Δ <i>minD minE</i> :: <i>sfgfp-minD minE</i> <> <i>kanR frt</i>	This work
FW1247	W3110, Δ <i>leuB</i> :: <i>Pj23100 tagBFP</i> <> <i>kanR frt</i>	This work
FW1489	W3110, Δ <i>leuB</i> :: <i>Pj23100 eqFP670</i> <> <i>kanR frt</i>	This work
FW1555	W3110, Δ <i>minD minE</i> :: <i>sfgfp-minD minE</i> <> <i>frt</i>	This work
FW1590	W3110, Δ <i>minD minE</i> :: <i>sfgfp-minD minE</i> <> <i>frt</i> , Δ <i>leuB</i> :: <i>eqFP670</i> <> <i>kanR frt</i>	This work
Plasmids		
pFX40	<i>Plac</i> :: <i>yfp-minD minE</i> (AmpR)	4
psfGFP	<i>Pt7</i> :: <i>sfgfp</i> (AmpR)	Partregistry *
pKD13	<i>kanR frt</i> (AmpR)	2
pBVS3	<i>Plac</i> :: <i>yfp-minD minE</i> <> <i>kanR frt</i> (AmpR)	This work
pBVS4	<i>Plac</i> :: <i>sfgfp-minD minE</i> <> <i>kanR frt</i> (AmpR)	This work
pDonR P4-P1R	Gateway plasmid entry 1	Invitrogen
pDonR 211	Gateway plasmid entry 2	Invitrogen
pDonR P2R-P3	Gateway plasmid entry 3	Invitrogen
pDEST R4-R3	Gateway destination vector	Invitrogen
pET-15a	<i>lacI</i> :: <i>Pt7</i> (AmpR)	Merk
pTagBFP-C1	<i>Pcmv</i> :: <i>TagBFP</i> (KanR)	Evrogen
pNirFP-N1	<i>Pcmv</i> :: <i>eqFP670</i> (KanR)	Evrogen
pBVS7	pDonR P4-P1R :: <i>lacI-Pt7</i>	This work
pBVS19	pDonR 221 :: <i>tagBFP</i>	This work
pBVS17	pDonR P2R-P3 :: <i>kanR frt</i>	This work
pBVS35	<i>pDEST</i> :: <i>lacI-Pt7 tagBFP kanR frt</i>	This work
pBVS28	pDonR P4-P1R :: <i>leuB</i> '- <i>Pj23100</i>	This work **
pBVS15	pDonR 221 :: <i>eqFP670</i>	This work
pBVS29	pDonR P2R-P3 :: <i>kanR frt-leuB</i> ''	This work **
pBVS33	<i>pDEST</i> :: <i>leuB</i> '- <i>Pj23100</i> :: <i>eqFP670</i> :: <i>kanR frt-leuB</i> ''	This work
pKD46	<i>Para</i> :: <i>Red</i> (AmpR)	2
pCP20	<i>Pr-flp</i> (AmpR CmR)	2
pKD3V	<i>cat frt</i> :: <i>sacB</i> (AmpR)	13 ¹³

* Source: http://parts.igem.org/Part:BBa_I746908

** *leuB*' and *leuB*'' denote the 200 bp sequences at the complementary strand of C-terminus region and N-terminus region of *leuB* gene.

Table 4. Parameters for the numerical simulations*

Parameters	Values	Descriptions
c_D	0.85 μM	Total concentration of MinD
c_E	0.31 μM	Total concentration of MinE
D_{DD}	16 $\mu\text{m}^2/\text{s}$	Diffusion constant of MinD.ADP _c
D_{DT}	16 $\mu\text{m}^2/\text{s}$	Diffusion constant of MinD.ATP _c
D_E	10 $\mu\text{m}^2/\text{s}$	Diffusion constant of MinE _c
D_d	0.013 $\mu\text{m}^2/\text{s}$	Diffusion constant of MinD.ATP _m
D_{de}	0.013 $\mu\text{m}^2/\text{s}$	Diffusion constant of MinDE _m complex
k_D	0.075 $\mu\text{m}/\text{s}$	Rate of direct binding of MinD.ATP _c to the membrane
k_{dD}	0.05 $\mu\text{m}^2/\text{s}$	Rate of recruitment of MinD.ATP _c by MinD.ATP _m
k_{dE}	0.25 $\mu\text{m}^2/\text{s}$	Rate of recruitment of MinE _c by MinD.ATP _m
k_{de}	0.33 s^{-1}	Rate of the dissociation of the MinDE _m complex
λ	1 s^{-1}	Rate of nucleotide exchange on MinD

* Note that the parameter values were converted according to the units set for deterministic simulations in VirtualCell

Supplementary Movies

S1. Single *E. coli* cells growing into user-defined cell shapes. Shown is the fluorescence of the cytosolic eqFP670.

S2. Min oscillations in rod-shape cells in a micro-colony. Shown are cytosolic eqFP670 (left) and sfGFP-MinD (right) fluorescence.

S3. Min oscillations in cells shaped into a rectangle, a square, a circle, and a triangle. Shown are one cytosolic image followed by time-lapse images of sfGFP-MinD.

S4. Min oscillations in square-shape cells with various sizes. Shown are one cytosolic image followed by a movie of sfGFP-MinD time-lapse images.

S5. Min oscillations in rectangular cells with sides between 2 and 4.5 μm . Shown are one cytosolic image followed by a movie of sfGFP-MinD time-lapse images, an SD image, and an overlay image of cytosol and SD.

S6. Min oscillations in rectangular cells with sides between 1 and 11 μm . Shown are one cytosolic image followed by a movie of sfGFP-MinD time-lapse images.

S7. Min oscillations showing examples of the 7 modes of MinD patterns in rectangular cells. Shown is the sfGFP-MinD fluorescence. Scale bar indicates 5 μm .

S8. Min oscillations in rectangular cells of around 10 μm showing pole-to-pole, 3-node stripe and 4-node stripe modes. These modes show similar oscillation period. Scale bar indicates 5 μm .

S9. Numerical simulation results showing that a simple reaction-diffusion model can recapture the major patterns observed experimentally.

S10. Numerical simulation results showing the effect of k_{dD} on the development of the polar-zone initiated asymmetrically in a cell of 5 μm x 3 μm x 1 μm . Shown is the surface view of the MinD.ATP molecules. The k_{dD} values of individual simulations are indicated, with a unit of $\mu\text{m}^2/\text{s}$.

S11. Numerical simulation results showing that the reaction-diffusion kinetics of Min proteins drive an initial diagonal concentration gradient to longitudinal oscillations. Shown is the 2D projection of MinD.ATP_m molecules in a 3D simulation in a cell of 3 μm x 2 μm x 1 μm . The simulation is carried out with a k_{dD} value of 0.025 $\mu\text{m}^2/\text{s}$.

S12. Numerical simulation results showing the effect of k_{dD} on sustaining diagonal patterns in rectangular cells with a width of 2 μm and different lengths. The lengths are shown in microns, and the k_{dD} values indicated have a unit of $\mu\text{m}^2/\text{s}$.

Note: All heatmaps in the movies share the same colorbars as in movie S4 – S7.

References

- 1 Pedelacq, J.-D., Cabantous, S., Tran, T., Terwilliger, T. C. & Waldo, G. S. Engineering and
2 characterization of a superfolder green fluorescent protein. *Nat. Biotech.* **24**, 79-88 (2006).
- 3 Datsenko, K. A. & Wanner, B. L. One-step inactivation of chromosomal genes in *Escherichia*
4 *coli* K-12 using PCR products. *Proc. Natl. Acad. Sci. U.S.A.* **97**, 6640-6645 (2000).
- 5 Shcherbo, D. *et al.* Near-infrared fluorescent proteins. *Nat Meth* **7**, 827-829 (2010).
- 6 Shih, Y.-L., Fu, X., King, G. F., Le, T. & Rothfield, L. Division site placement in *E. coli*:
7 mutations that prevent formation of the MinE ring lead to loss of the normal midcell arrest of
8 growth of polar MinD membrane domains. *EMBO J.* **21**, 3347-3357 (2002).
- 9 Shannon, C. E. A mathematical theory of communication. *Bell System Technical Journal* **27**,
10 379-423 (1948).
- 11 Fange, D. & Elf, J. Noise-induced Min phenotypes in *E. coli*. *PLoS Comput Biol* **2**, e80
12 (2006).
- 13 Halatek, J. & Frey, E. Highly canalized MinD transfer and MinE sequestration explain the
14 rigid of robust MinCDE-protein dynamics. *Cell Rep.* **1**, 741-752 (2012).
- 15 Bendezú, F. O. & de Boer, P. A. J. Conditional Lethality, Division Defects, Membrane
16 Involution, and Endocytosis in *mre* and *mrd* Shape Mutants of *Escherichia coli*. *J. Bacteriol.*
17 **190**, 1792-1811 (2008).
- 18 Hu, Z., Gogol, E. P. & Lutkenhaus, J. Dynamic assembly of MinD on phospholipid vesicles
19 regulated by ATP and MinE. *Proc. Natl. Acad. Sci. U.S.A.* **99**, 6761-6766 (2002).
- 20 Hsieh, C.-W. *et al.* Direct MinE-membrane interaction contributes to the proper localization
21 of MinDE in *E. coli*. *Mol. Microbiol.* **75**, 499-512 (2010).
- 22 Ivanov, V. & Mizuuchi, K. Multiple modes of interconverting dynamic pattern formation by
23 bacterial cell division proteins. *Proc. Natl. Acad. Sci. U.S.A.* **107**, 8071-8078 (2010).
- 24 Hayashi, K. *et al.* Highly accurate genome sequences of *Escherichia coli* K-12 strains
25 MG1655 and W3110. *Mol. Syst. Biol.* **2**, doi:10.1038/msb4100049 (2006).
- 26 Zhou, Q.-M., Fan, D.-J., Xie, J.-B., Liu, C.-P. & Zhou, J.-M. A method for generating precise
27 gene deletions and insertions in *Escherichia coli*. *World J. Microbiol. Biotechnol.* **26**, 1323-
28 1329 (2010).